Journal of Materials Chemistry A

PAPER

Cite this: J. Mater. Chem. A, 2017, 5, 7200

Percolation of a metallic binder in energy generating composites†

Kelsey Meeks,[ab] Dylan K. Smith,[a] Billy Clark[c] and Michelle L. Pantoya *[a]

Received 20th January 2017
Accepted 13th March 2017

DOI: 10.1039/c7ta00689f

rsc.li/materials-a

Indium is introduced here as a metallic binder in energetic composites as an approach for consolidating the media and providing a highly conductive percolating scaffold for enhancing energy transport. Indium can replace traditional polymer binders and provide an approach for not only binding composites but also enhancing energy transport. For energy generation applications, a commonly used formulation in thermal batteries is investigated and comprised of magnesium (Mg) and manganese dioxide (MnO_2) powders mixed with varying indium (In) concentrations and pressed into thin sheets. Scanning electron microscopy (SEM) images indicated that during compression In flows through voids in the composite, resulting in a connected network of highly conductive filler. This network produces self-adhered composites that do not require additional binders. The thin sheets are ignited, flame speeds are measured, and specific energy ranged from 2000–5000 kJ kg^{-1} depending on the In concentration. Energy liberation is maximized for Mg + MnO_2 mixed with 19 vol% In. Laser flash analyzer (LFA) thermal conductivity measurements demonstrate a good correlation between high energy propagation rates and optimal thermal conductivity. However, increased thermal conductivity is balanced by decreased heat production, and energy propagation decreased beyond 19 vol% In. Comparison of thermal conductivity measurements with predictions from classical and more recent percolation theories show that percolation in composites most closely aligns with the assumptions of the lattice percolation theory.

1. Introduction

Composites consisting of a reacting metal and metal oxide pair can produce reactions characterized by a high exothermicity, good energy density, and low to moderate gas generation. Understanding ignition and propagation of these reactions is important for their optimization in energy generating applications.[1] Mechanisms such as random walk of hot particles,[2] convective flow of hot gasses,[3,4] and thermal conduction[5,6] have been demonstrated to have varying degrees of importance in different composites. For composites of aluminum and copper oxide (Al + CuO), increasing composite density resulted in a shift from convection dominated flame propagation to conduction dominated flame propagation.[7] Sullivan *et al.* proposed that the advection of hot particles played a key role in the energy transport of nanocomposite thermites and increasing composite thickness resulted in a transition of the energy transport mechanism from conduction to hot particle advection.[8] Several studies highlight the importance of intimate contact between the fuel and the oxidizer (*e.g.*, small mass diffusion distances) for efficient propagation of energetic reactions.[6,9–12] These findings are interesting and reveal that propagation of energy through an energetic composite is dependent not only on reaction kinetics, but also on the composite morphology and packing density and even composite thickness can affect reaction mechanisms. Previous research on Mg–MnO_2 added fillers to generate well adhered coatings with flame speeds on the order of 100 cm s^{-1} for thermal battery applications.[13,14] These studies also found a decrease in the flame speed with increasing binder concentration, attributed to decreased thermal transport properties from a low binder thermal conductivity.[14]

Indium (In) is a ductile, post transition metal with a low melting point (157 °C), high thermal conductivity (81.8 W m^{-1} K^{-1} (ref. 15)) and low electrical resistivity (8.1 μΩ cm (ref. 16)). These properties have led to use of In (often in the form of indium tin oxide) in a variety of applications, including organic light emitting devices,[17] semiconductors,[18] soldering,[19] and microelectronics.[20] Indium is also notable for its ductility, and eutectic alloys containing indium have been shown to behave as an elastic material until subjected to a threshold surface stress, after which In flows like a liquid.[21] Here, the malleability and high thermal conductivity make In a feasible alternative to traditional polymer binders and an ideal filler for controlling thermal properties.

Although the practice of adding a filler or interstitial phase material to energetic composites has been of general interest for some time, it has been the subject of focused study for energetic

[a]Mechanical Engineering Department, Texas Tech University, Lubbock, TX 79409-1021, USA. E-mail: michelle.pantoya@ttu.edu

[b]Sandia National Labs, Albuquerque, NM 87185, USA

[c]BiSN Oil Tools, 4539 Brittmoore Rd., Houston, TX 77041, USA

† Electronic supplementary information (ESI) available. See DOI: 10.1039/c7ta00689f

composites for the past several decades. Fluoropolymer binders (or fillers) have been added to many composites to improve their mechanical properties.[22] Recently, binders such as polytetrafluoroethylene (PTFE or Teflon™),[23] paraffin,[24] Viton® fluoroelastomers,[25,26] and polyvinylidene fluoride (PVDF)[27] have been added to energetic materials to create well-adhered coatings with reasonable flame speeds and energy densities. In some deposition methods, such as those introduced by Clark *et al.*, these binders can be used to create free standing films of flexible energetic materials.[23] These efforts could also advance the development of 3D printing of energetic materials. Other work focused on using fillers to improve the ESD sensitivity,[28] microwave energy absorption[29] or thermal transport properties of energetic material composites.[30,31] A key to understanding the mechanical and heat transport properties of these composites lies in the analysis of particle connectivity within these matrices.

Although a robust analysis of particle connectivity in real composite materials has historically proven difficult due to the highly variable structure of most powder composites, the study of particle connectivity has a rich history in the analysis of idealized systems. The work of Scher and Zallen in the 1970s postulated the existence of an invariant percolation threshold for two-dimensional lattices occupied by disks of uniform radius, independent of the disk radius or specific lattice geometry.[32] Further work found similar invariants for spheres in three dimensional systems. With the implementation of Monte Carlo simulations, prediction of percolation thresholds for a variety of different particle shapes in two and three dimensional continuums was made possible with increasing accuracy.[33] Many current efforts in this area focus on the prediction of percolation thresholds for systems more authentic to real world systems, including factors such as polydispersity and interpenetration.

Classical percolation theory describes the effective bulk connectivity of the filler material as a binary, wherein below the percolation threshold bulk connectivity across the matrix does not exist, and above the percolation threshold connectivity spanning the system is a near statistical certainty. These models describe two distinct macroscopic composite states – below or above the percolation threshold – with little to no transition. For many real systems, these models can be used to accurately describe the bulk composite behavior. For example, in electrically insulating epoxy matrices, the addition of an electrically conductive filler results in a rapid transition from bulk isolation to conduction at the percolation threshold.[28,34,35]

However, as noted by several researchers[31,36,37] in the case of thermal conductivity, although classical percolation models are helpful in the prediction of behavior, they do not fully describe the observed results. These studies have also noted that the thermal conductivity in composites is often more complex than a simple weighted average model would suggest,[36] although a more complex model was presented by Nielsen *et al.*[38] Here, we will show that the behavior of thermal conductivity in composites falls somewhere between percolation theory and the weighted average model.

The goal is to introduce a highly conductive liquid metal filler as a reactant in the energetic formulation to serve multiple purposes: (1) act as a binder facilitating consolidation of powder media; and (2) enhance energy transport and reactivity. The objective is to determine the effect of a thermally conductive In filler on the reactivity of Mg–MnO_2. To that end, powders of Mg and MnO_2 were mixed with varying In powder concentrations and pressed into self-adhered thin sheets. These composites were pressed to high bulk densities and, due to the unique properties of In, pressing resulted in thin sheets that maintain their shape without requiring the addition of a supplemental filler material (*i.e.*, no additional binder is needed to consolidate the composite). The thin sheets were investigated to assess their flame speed and thermal properties. Concepts from percolation theory were applied to the results to determine how predictions of behavior could be extended to energetic material composite systems.

2. Experimental procedure

Magnesium and manganese dioxide powders were prepared stoichiometrically with varied concentrations of indium powder to form composites (Mg–MnO_2–In). The Mg–MnO_2 reaction – shown in reaction (1) – is a theoretically moderately gas generating reaction with a high flame temperature and high energy density (*i.e.*, gas generation is 0.41 mg per mg reactant; the flame temperature without phase change is 5209 K and the heat of combustion is 5531 J g^{-1} from ref. 39).

$$2Mg + MnO_2 \rightarrow 2MgO + Mn \quad (1)$$

The experimental procedure for each tested sample consisted of a mixing step and a pressing/assembly step. Pressing was followed by flame speed measurements or thermal conductivity measurements, depending on the type of sample produced.

2.1 Materials and mixing

Magnesium and manganese dioxide were obtained from Alfa Aesar as micron sized particles and sieved through a −325 mesh, and indium was obtained from Sigma Aldrich and sieved through a −100 mesh. These meshes filter out particles larger than 44 and 140 microns, respectively. As such, the mesh size provides an indication of the largest potential particle size in the powder, but not the average or range of particle sizes. In order to better characterize the particle size distributions of the powders, a particle size analyzer was used (Particle Sizing Systems Model number 780V SIS Sensor mode Summation). The particle analyzer determined the size of each particle in a powder sample using a light obscuration sensor and reported the mean and standard deviation based on a population differential distribution. Statistics on particle sizes are reported in Table 1, and the particle sizes determined by the analyzer for each powder sample are listed in the ESI.† The powders were suspended in filtered water (approximately 1 mg powder per 100 mL of water) and sonicated for 2 minutes with a 50% duty cycle to break up agglomerates. The resultant mixture was then pulled using a syringe pump into the size analyzer. The length of each particle was measured to a resolution of 10 nm, and

Table 1 Particle size diameter summary

	Mean (μm)	Mode (μm)	Median (μm)	Std deviation (μm)	Range
In	2.7	1.5	2.1	1.9	0.5–500
MnO_2	4.1	4.1	3.6	2.3	0.5–500
Mg	8.9	8.6	7.1	6.9	0.5–500

statistics were reported using a count based averaging. All powders had a mean particle diameter in the micrometer range, and no measured particle exceeded 130 μm in diameter.

The Mg and MnO_2 powders were measured to a stoichiometric ratio of one and mixed with the specified mass of In powder. Isopropanol was then added such that the final slurry was 30% solids by volume. This slurry was mixed in a centripetal planetary mixer (AR250, Thinky, Japan) at 1500 rpm for four minutes. After mixing, the slurry was flushed from the mixing container using excess isopropanol and dried in a Pyrex dish in a vacuum oven set to 110 °C for at least 30 minutes. The powders were then scraped in a fume hood using a ground razor blade and reclaimed for further experimentation.

2.2 Pressing and processing

Thin sheets and pellets were prepared by pressing in two different dies using a hydraulic press and an applied pressure of 7000 kPa. For flame speed measurements, thin sheets were prepared using a custom stainless steel press, as shown in Fig. 1. This press produced thin sheets 0.635 cm wide and 6.985 cm in total length, and shimmed to a height of 0.889 cm. The resultant thin sheets were free standing, and mechanically stable enough to be moved and tested without the need for an additional binder. However, the thin sheets were somewhat brittle, and careful handling was required.

Samples pressed for laser flash analyzer (LFA) thermal conductivity measurements were prepared using a cylindrical die to produce pellets with a diameter of 12.5 mm and a thickness of 1.7 mm.

Indium concentration varied from 9 to 38 vol% of the mixed powder. For all samples, powder was added such that the consolidated sample had a TMD of 70% and an In concentration between 6 and 27 vol%. Detailed discussion of TMD calculation and bulk density determination is provided in the ESI† section of this paper. The appropriate mass of powder was added to the press and gently leveled with a metal spatula. Shims were applied and the material was pressed until the plunger head of the pellet press and shims were flush. The base plunger of the pellet press was removed, and the sample was ejected from the press. The final sample was massed and measured, the resultant density recorded, and % TMD calculated. The LFA samples were coated with a dry graphite film lubricant to facilitate absorption of incident radiation.

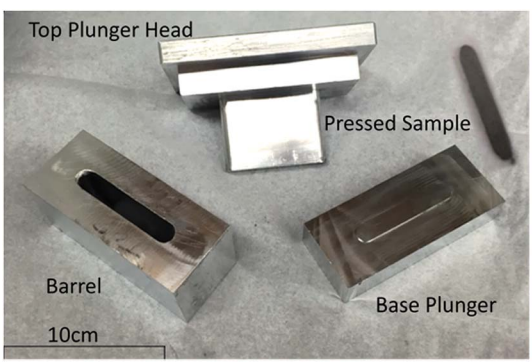

Fig. 1 Photograph of the stainless steel press used to form energetic thin sheets.

2.3 Flame speed measurements

Flame speeds were measured using a high speed Photron Fastcam camera. Samples were placed in the firing chamber onto a highly thermally insulating brick at ambient pressure and temperature. Ignition was achieved by a small gage nichrome hot wire. The camera was positioned perpendicular to the direction of flame propagation and set to record at a frame rate of 1000 fps, an f-stop of 32 and an exposure of 7 microseconds. Neutral density filters were placed on the camera lens so that the resultant images could be processed without sensor saturation. Calibration shots were taken before and after firing, and post-processing was completed using the Photron software.

2.4 Thermal conductivity measurements

The thermal conductivity, k, is calculated using eqn (2), assuming that the thermal diffusivity, α, specific heat capacity, C_p, and the density, ρ, are known.

$$k = \alpha C_p \rho \tag{2}$$

The density of each sample was calculated after pressing, and thermal diffusivity and the specific heat capacity were measured using a Netzsch LFA 447 Nanoflash Laser Flash Analyzer (LFA). The LFA measures thermal properties using the flash diffusivity method, wherein samples are heated by using a xenon flash lamp in a parabolic mirror. This flash lamp emits a 115 or 230 V, 10 A, 50/60 Hz light pulse directed at the sample. The temperature of the sample is measured by using a liquid-nitrogen cooled indium antimonide infrared detector. The time elapsed for the sample to reach 50% of its target value, t_{50}, is reported and used to calculate the thermal diffusivity as shown in eqn (3) with l defined as the thickness of the sample.[40]

$$\alpha = 13.88\frac{l^2}{t_{50}} \tag{3}$$

The specific heat capacity of the sample is determined simultaneously using eqn (4) by comparing the heat rise of the sample to the heat rise of a Pyroceram™ reference sample with a known specific heat capacity.

$$C_{p_{sample}} = \frac{(mC_p\Delta T)_{ref}}{(m\Delta T)_{sample}} \tag{4}$$

Eqn (3) and (4) enabled calculation of the thermal conductivity, as given in eqn (2). For each In concentration, two to three samples were prepared, and each thermal diffusivity and specific heat capacity measurement was repeated five times and averaged for a final reported value consisting of 10 to 15 data points. Analysis and determination of the thermal conductivity was aided by the Netzsch Proteus software.

3. Results

3.1 Composite morphology

The morphology of the Mg–MnO_2–In composites was examined in an SEM in order to characterize the microstructure. The SEM images were captured for batches of powder containing 15 vol% In in the loose powder (10 vol% when pressed to 70% TMD) before and after pressing, as shown in Fig. 2. These images are of the top surface of the powder or thin sheet, and indicate good dispersions and mixing of Mg–MnO_2–In.

There are a few interesting observations from these images. The most gripping is the radical morphology change undergone by the In during pressing. Although indium is a roughly spherical powder prior to pressing, as shown in Fig. 2a, during pressing it is deformed into large, contiguous agglomerates, as depicted in Fig. 2b. This is consistent with the unique properties of soft metals such as indium and gallium, where materials behave like an elastic material until a critical surface stress is exceeded, at which point they display properties of a liquid.[21] Fig. 2b shows the stress from pressing "flows" In through microchannels in the Mg–MnO_2 matrix, and achieves not only a new structure, which binds the composite into thin sheets, but may achieve a better dispersion of In in the system. This has some interesting implications on the thermal conductivity of the resultant mixture, as shall be discussed shortly.

3.2 Flame speed measurements

Fig. 3 shows the flame speed measurement as a function of the In concentration. Each In concentration was tested with at least two and a maximum of six samples. All samples were mixed to a solid concentration of 30 vol% and an equivalence ratio of one for the Mg–MnO_2 reactants. These samples were shimmed before pressing to a height of 0.889 cm and pressed to 70% TMD. Two different firing conditions were used for this study (approximately a third of the shots were fired on a stainless steel block instead of on a thermal brick). The high thermal conductivity of the stainless steel relative to the thermal brick resulted in differing values of the flame speeds: the stainless steel block effectively wicked heat away from the reaction, resulting in slower flame speeds. However, both firing configurations exhibited distinctly similar trends. From Fig. 3, the flame speeds are maximized for pressed thin sheets containing 14 vol% In, and the flame speed decreases away from this threshold.

3.3 Thermochemical calculations

Fig. 4 shows the theoretical heat of combustion and the adiabatic flame temperature as a function of In concentration as determined by the thermochemical equilibrium code REAL (Timetec L.L.C.).[41] Heat of combustion simulations assume a constant specific volume of 0.01 m^3 kg^{-1} and a specific internal energy of zero. The adiabatic flame temperature was calculated assuming a constant pressure of 101.325 kPa and a specific enthalpy of zero. These calculations assume that the reaction is complete and adiabatic with no energy loss and represents an ideal upper limit of the heat of combustion for the simulated reaction. This software has previously demonstrated good agreement between the simulated and the experimentally measured adiabatic flame temperature.[4]

From the thermochemical equilibrium simulations presented in Fig. 4, as the In concentration increases, the theoretical heat of combustion and adiabatic flame temperature decrease, exhibiting a very different trend than that seen in Fig. 3. In general, the principal reaction products are MgO and Mn, with small quantities of various indium oxides. This indicates that In did not substantially participate in the reaction, although it constituted a parasitic load resulting in decreased heat production and flame temperature. The increase in the

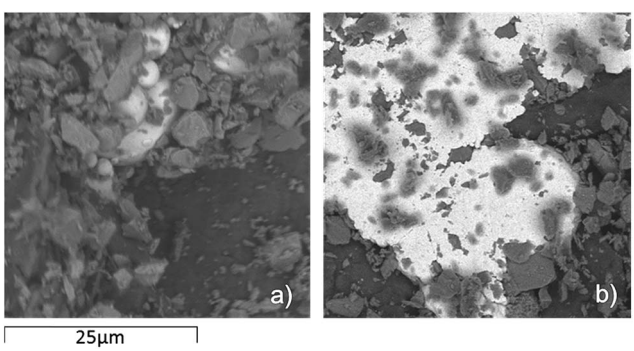

Fig. 2 Backscatter SEM images of Mg–MnO_2 containing 15 vol% In (a) before pressing and (b) after pressing. The low *Z*-number indium appears as the brighter particles in these images, and clearly undergoes plastic deformation consistent with "flowing" during the pressing process.

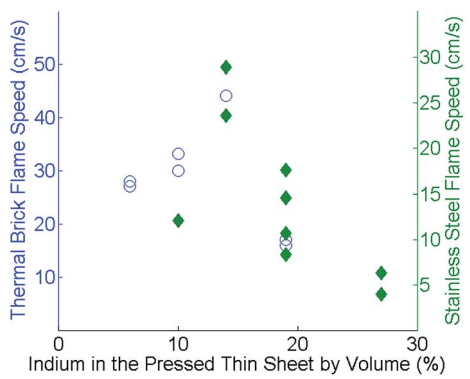

Fig. 3 Flame speeds of Mg–MnO_2–In thin sheets as a function of varying In concentration. Open circles denote samples fired on a thermal brick, and closed diamonds denote samples fired on the stainless steel substrate. An In concentration of 14 vol% results in the highest flame speeds.

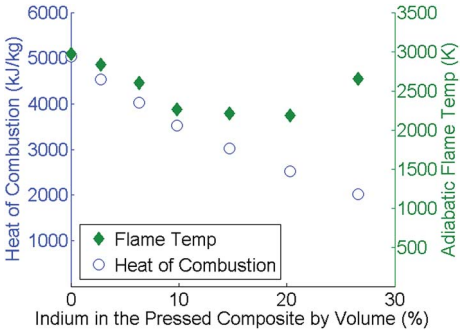

Fig. 4 Theoretical heat of combustion (open circles) and adiabatic flame temperature (closed diamonds) from REAL code simulations. These simulations show a decrease in the heat of combustion with an increased In concentration, and a general decrease in the adiabatic flame speed.

simulated adiabatic flame temperature from 19 to 27 vol% In is likely due to a decrease in predicted vapor phase indium.

3.4 Thermal conductivity and diffusivity

Fig. 3 naturally raises some questions about how the thermal transport properties of the composite change with varying In concentration. In order to better characterize the thermal transport properties of the composite, thermal conductivity was measured using the LFA as described above. All results represent the average of three samples, except the 14 vol% In, for which only two samples were tested. Fig. 5 shows the resultant thermal conductivity measurements, as a function of varying In concentration in the final mixture by volume. All pellets were prepared to an equivalence ratio of one for the Mg–MnO_2 powder, and shimmed to a height of 1.7 mm resulting in pellets with bulk densities of 70% TMD.

From Fig. 5, it can be seen that higher In concentration results in higher thermal conductivities – unsurprising given the high thermal conductivity of In (81.8 W m^{-1} K^{-1} from ref. 15) relative to the fixed concentration and thermal conductivities of manganese dioxide (4.0 W m^{-1} K^{-1} from ref. 44) and magnesium oxide (30–60 W m^{-1} K^{-1}),[45] which likely constitute the passivated outer shell of the magnesium particles and magnesium (156 W m^{-1} K^{-1}).[15] The rate of this rise increases rapidly between 10 and 14 vol% In concentration.

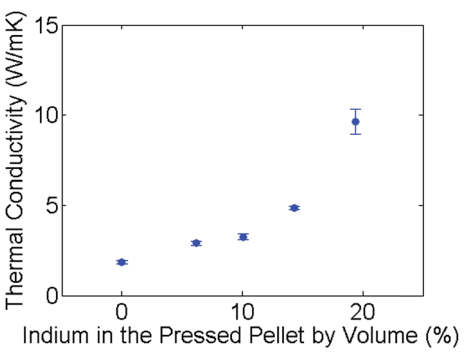

Fig. 5 Thermal conductivity as a function of In concentration in the Mg–MnO_2–In composite. The shape of this graph is consistent with percolating thermal conductivity models in the literature.[31,42,43] The error bars represent the standard deviations from repeatability of 2–3 samples, and represent the highest uncertainty in the data.

The measured thermal conductivity of the Mg–MnO_2–In composite (Fig. 5) can be compared to the effective thermal conductivity model for composites, previously applied by Smith *et al.*[31] and Vargas *et al.*[29] to energetic materials, wherein the Hashin–Shtrikman (HS)[42,43] model is used to predict the upper and lower bounds of thermal conductivity for a two phase matrix with no porosity. The upper bound, HS+, describes a composite consisting of a high thermal conductivity matrix with a thermal conductivity of k_H and a low thermal conductivity filler with thermal conductivity given by k_L, and is given in ref. 46 and in eqn (5).

$$\mathrm{HS}+ = k_H \frac{2k_H + k_L - 2X_L(k_H - k_L)}{2k_H + k_L + X_L(k_H - k_L)} \quad (5)$$

The corollary lower bound, HS−, describes a composite consisting of a low thermal conductivity matrix, (k_L), with a high thermal conductivity filler (k_H), and is given by eqn (6).

$$\mathrm{HS}- = k_L \frac{2k_L + k_H - 2X_H(k_L - k_H)}{2k_L + k_H + X_H(k_L - k_H)} \quad (6)$$

where X is the volume fraction of the high thermal conductivity material (X_H) or low thermal conductivity material (X_L).

For a given ratio of high and low thermally conducting materials, a value of interconnectivity can be calculated from the Hashin–Shtrikman upper and lower bounds using a method described by Schilling and Partzsch[47] given in eqn (7), where $k_{measured}$ is the experimentally measured thermal conductivity.

$$X_{interconnected} = \frac{k_{measured} - k^{HS-}}{k^{HS+} - k^{HS-}} \quad (7)$$

Although the composite is Mg, MnO_2, In, and air, for this analysis the matrix is treated as a two phase composite with the thermal conductivities of Mg, MnO_2 and air comprising the first phase (the lower thermal conductivity matrix) and the thermal conductivity of In is the second phase (the higher thermal conductivity filler). By taking the measured thermal conductivity of a pellet with no added In (*i.e.*, 1.8 W m^{-1} K^{-1} from Fig. 5) as k_L and the thermal conductivity of In (81.8 W m^{-1} K^{-1} from ref. 15) as k_H, the upper and lower bounds of the thermal conductivity per eqn (5) and (6) are calculated and plotted with the measured thermal conductivity as a function of the volume concentration of In to generate Fig. 6.

In Fig. 6 the experimentally measured thermal conductivity of Mg–MnO_2–In lies between the upper and lower Hashin–Shtrikman bounds, in keeping with the theory. Additionally, the thermal conductivity of the measured composite is fairly close to the HS− lower bound until around 14 vol% In, and grows much closer to the HS+ upper bound near 19 vol%. To further illustrate this, the interconnectivity of In in the matrix was approximated using eqn (7), and plotted in Fig. 7.

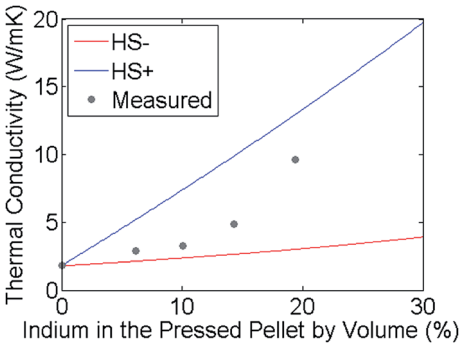

Fig. 6 Experimentally measured thermal conductivity of Mg–MnO_2–In pellets as a function of In concentration, as well as the upper and lower bounds of the thermal conductivity predicted by eqn (5) and (6).

From Fig. 7, the interconnectivity of In substantially increases after 14 vol%. It is difficult to say exactly when percolation of In within the composite occurs. From the high value of thermal conductivity and interconnectivity, bulk connected components of In likely exist within the composite at 19 vol% In, although from the data and trends it is unclear whether percolation of In has occurred at 14 vol%, and this volume loading may be near the percolation threshold for this composite. The value of interconnectivity given in Fig. 7 is an approximation of the particle connectivity in the composite derived from the theoretical bounds given by the HS model. The apparent slight dip in interconnectivity between 6 and 10 vol% is most likely due to complexities in the multiphase composite not captured by the HS model.

Fig. 7 taken together with Fig. 3 and 5 indicates that the highest flame speeds occur very close to the onset of percolation of In in the composite, but not at the highest interconnectivities of In. This can be compared to the predictions of the percolation threshold from classical theory and recent advances.

3.5 Comparison of experimental results to percolation theory

From classical lattice percolation theory, the percolation threshold for spheres in a lattice (no interpenetration) is 16 vol% for a square lattice.[48] For continuum systems of interpenetrating disks of a single radius, the total volume fraction is 0.3418, and the covered volume fraction is 0.2895 (or 28.95 vol%).[33,49,50] It has been postulated that for monodisperse systems of particles with an arbitrary shape, the percolation threshold in the three dimensional continuum is governed by a constant excluded area fraction of between 0.7 and 2.8.[51] Meeks *et al.* extended this concept to polydisperse systems, and proposed that the pairwise excluded volume is a constant for two and three dimensional systems at percolation.[52] Their main hypothesis is represented by eqn (8), where n_c is the number density of the objects at percolation, f is the probability of occurrence for an object of the i^{th} type, V_{ij} is the pairwise excluded volume of objects i and j, and $\eta_{ex,c}$ is the constant excluded volume, a quantity given by $\eta_{ex,c} = 8\eta_{c,3} = 8 \times 0.2895$.

$$\eta_{ex,c} = n_c \sum f_i f_j V_{ij} \quad (8)$$

For three dimensional spheres, the quantity V_{ij} is given by eqn (9)

$$V_{ij} = \frac{4}{3}\pi(R_i + R_j)^3 \quad (9)$$

For particles with a known size distribution, such as the size distribution of the powdered In used in this study given in the ESI,† n_c can be calculated from eqn (8) and (9). This can then be used to calculate the filler fraction at percolation by eqn (10), where V_{eff} is the average volume of a particle, given by eqn (11).

$$\eta_c = n_c V_{eff} \quad (10)$$

$$V_{eff} = \sum_i f_i V_i \quad (11)$$

This theory was shown to capture some trends of two disk systems; however, Meeks *et al.*,[52] suggested that the percolation of such systems could more accurately be predicted if the volume fraction, v, was used *in lieu* of the probability f to calculate n_c. For three dimensional spheres, the volume fraction is given by eqn (12).

$$v_i = \frac{R_i^3 f_i}{\sum_j R_j^3 f_j} \quad (12)$$

By subsisting v into eqn (8) and (11) in place of f, the number density of objects at percolation can be calculated by eqn (13), and then the percolation threshold by eqn (9) and (10).

$$\eta_{ex,c} = n_c \sum v_i v_j V_{ij} \quad (13)$$

In a subsequent study, Meeks *et al.*[53] suggested that the predictions of percolation thresholds could be further refined by including a size correction factor and a density correction factor. For binary disk dispersions in two dimensions, they suggested a size correction factor given by eqn (14) and a density correction factor by eqn (15).

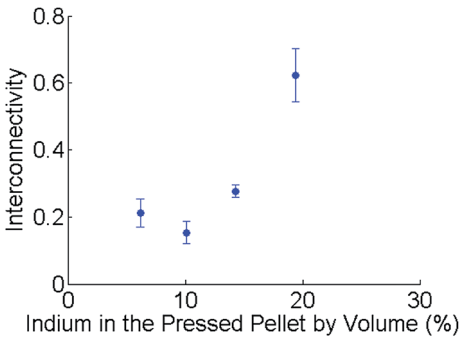

Fig. 7 Interconnectivity of indium in the Mg–MnO_2 matrix. Interconnectivity of indium increases sharply between 14 and 19 vol% In.

$$\beta_i = \left(\frac{R_i}{R_{\max}}\right)^{2/3} \quad (14)$$

$$\gamma_i = \frac{f_i\left(\frac{R_i}{R_{\max}}\right)^2}{f\left(\frac{R_i}{R_{\max}}\right)^2 + (1-f)^{\frac{3}{2}}} \quad (15)$$

These correction factors show very good agreement with the Monte Carlo results for two dimensional binary disk dispersions. These correlations can be extended to the system discussed here, where the size correction factor is implemented in the calculation of the average excluded area, given by eqn (16).

$$V_{ij}(\beta_i, \beta_j) = \frac{4}{3}\pi(\beta_i R_i + \beta_j R_j)^3 \quad (16)$$

The density correction factor is substituted in place of f in eqn (8) and (11). The critical number density at percolation is then given by eqn (17).

$$\eta_{ex,c} = n_c \sum \gamma_i \gamma_j V_{ij}(\beta_i, \beta_j) \quad (17)$$

Taking the size distribution given for indium particles in Table S1 in the ESI,† the critical number of disks can be calculated by eqn (8), (13), or (17), and the percolation threshold for each method by eqn (9)–(11). The results of these calculations and the predictions for monodisperse spheres in the lattice and continuum systems are listed in Table 2. The calculations listed in Table 2 exclude any particle size found by the particle size analyzer with fewer than ten particles reported.

From these results, the prediction of the percolation threshold from lattice theory is most consistent with the behavior of In in these systems. However, both the lattice and continuum percolation theory contain assumptions which may or may not be accurate for this system. The values of the percolation threshold reported in Table 2 for both the lattice and continuum percolation assume monodisperse, perfectly spherical objects dispersed completely at random. Although the In particles are assumed to be roughly spherical prior to pressing, slightly oblong objects would have lowered percolation thresholds. Additionally, neither theory accounts for settling, deformation during pressing, or other mixing effects. Lattice percolation assumes that only some positions are available for occupancy, and the percolation value reported in Table 2 assumes that these lattices are regular. Continuum percolation assumes that the dispersed objects would be able to interpenetrate, which would not be possible for hard-shelled objects such as In. This can be somewhat accounted for by considering the covered area fraction, ϕ_c, *in lieu* of the total volume fraction, η_c, but from Table 2 it is clear that even these values are biased high. Therefore, it seems likely that the underlying assumption of continuum systems – that any point is available for occupancy in the system – is less consistent with the observed behavior of mixed, hard shelled particles than the assumptions of lattice percolation.

We additionally note that although eqn (8) and (13) do not correlate with the observed experimental results, they produce plausible values of ϕ_c and η_c, indicating that the theory put forth by Meeks *et al.* in ref. 53 may be extended to polydisperse three dimensional systems. However, the percolation threshold predicted by eqn (17) seems implausibly high, indicating that the correction to the theory suggested in ref. 53 cannot be extended to three dimensional systems.

Table 2 Percolation threshold of In distribution as predicted by multiple theories. The quantity η_c represents the critical total volume of all objects, and ϕ_c the critical volume fraction

Percolation result	Source	η_c	ϕ_c
Measured indium percolation	Fig. 7	0.14–0.19	0.14–0.19
Percolation prediction method	**Source**	η_c	ϕ_c
Monodisperse disks	Lattice theory	0.16	0.16
Monodisperse disks	Continuum theory	0.3418	0.2895
Meeks method	Eqn (8)	0.55	0.42
Meeks modified method	Eqn (13)	0.43	0.35
Meeks Tencer method	Eqn (17)	0.66	0.48

4. Discussion

The results show that flame speeds for energetic material reactions can be increased by the addition of In powder. Flame speeds are increased by 35% by increasing the In concentration from 6 to 14 vol% (Fig. 1). This increase in reactivity follows a trend of increasing thermal transport properties (Fig. 5), but a trend of decreased theoretical heat production and adiabatic flame temperature (Fig. 4). This indicates that thermal conduction plays a key role in energy transport through the reacting composite, and that increasing thermal conduction of the composite increases flame speeds, even in the face of decreased overall heat production.

However, it is clear that there is a limit to this benefit, because the flame speed decreases rapidly for In concentrations in excess of 14 vol%. The increase in thermal transport properties (Fig. 5) is balanced by the reduced overall energy of the reaction (Fig. 4). In addition to the decreased available thermal energy, participation of In in the reaction is likely parasitic. Many studies have shown that good mixing of the fuel and oxidizer (short mass diffusion distances) is critical to reaction propagation for energetic materials.[6,9–11] As the volume of In in the energetic composite is increased, In will begin to inhibit contact between the fuel and oxidizer particles which will decrease reactivity by increasing mass diffusion distances. Here the effect of this interference may increase sharply shortly after In achieves percolation, at this threshold large connected components of In are prevalent within the matrix.

This supposition is consistent with the results of this study, because an In concentration of 19 vol% is consistent with the approximate onset of percolation of In in these materials (Fig. 5 and 6) and also produces the highest flame speeds (Fig. 3). Taken with the flame speeds shown in Fig. 3, the results indicate a distinct advantage to thermal transport in the composite, which translates to increased flame speeds. Once percolation is achieved, the benefit of the added thermal conductivity is greatly reduced when weighed against the reaction load of the increased parasitic material, in spite of increases in thermal conductivity.

Although there is a correlation between high thermal conductivities and flame speeds for Mg–MnO_2, other energetic composites may demonstrate different behaviors. Studies have shown that increasing the compaction density leads to decreased reaction rates for compositions with relatively high gas generation, suggesting a shift in the heat propagation mechanism from convection to conduction.[8,54] For such composites, the benefits of increased thermal conductivity provided by the indium filler will be balanced by the effect of compaction on reaction propagation, as the resultant high bulk densities inhibit convective energy transport. Intermetallic reactions, however, generate very little gas during reaction,[39] and represent an interesting, gasless alternative to the thermite composition studied here. Increasing the compaction density and thermal conductivity of such reactions may demonstrate even greater increases in flame speeds than those reported here.

We also note how the morphology changes in Fig. 2 imply changes in thermal conductivity observed in Fig. 5. Several studies have shown that thermal conductivities of composite materials – particularly those composed of compacted particles – often have lowered thermal conductivity due to the contact resistance between interfacial materials.[30,55–57] However, due to the morphological change in the In during the pressing process, the In particles appear less consistent with a series of small, contacting particles, and more consistent with a single percolating monocrystal. This suggests that the heat wave may propagate more efficiently though the percolating In matrix partly because the unique liquid-like structure greatly reduces the adverse effects of contact resistance between particles, in addition to the high thermal conductivity of In. It is difficult to determine how the morphology of In affects the thermal conductivity of the composite compared to its relatively high thermal conductivity with respect to the rest of the composite materials; however, it is probable that both of these factors affect the observed increase in conductivity, particularly given that the values of interconnectivity demonstrated in this paper are unusually high. Published results from similar studies have reported values of interconnectivity closer to 0.015–0.3, compared to 0.66 from this work, for similar volume concentrations (~14–19 vol%).[31,46,58,59] The high values of interconnectivity are likely due to the unique structure of the deformed In (Fig. 2b).

5. Conclusions

A liquid metal binder is introduced to improve the thermal properties of powdered energetic materials in the form of indium (In), a highly thermally conductive metal which deforms easily with the application of pressure. Pressing powdered reactants also forces In to "flow" through the powder and consolidate the media into free standing thin sheets. Increasing In concentration results in increasing thermal conductivity of the composite. The jump in thermal conductivity around 14 vol% In indicates percolation in the composite near or after this concentration. This percolation threshold is consistent with the predictions for In obtained by the application of traditional lattice percolation theory. Measurements showed increases in the flame speed up to this percolation threshold and decreases after percolation was achieved. Optimized In concentrations have energy densities on average of 3500 kJ kg^{-1}. This demonstrates that flame speeds for powdered energetic materials can be improved by the addition of highly thermally conductive fillers, and further suggests that this benefit is balanced by the increase of material parasitic to the reaction. It is supposed, but not conclusively proven, that the optimal balance of filler concentration will be the point at which percolation of the thermally conductive filler is achieved.

Acknowledgements

The authors gratefully acknowledge the advice of Dr John Tencer on the percolation calculations. Sandia National Laboratories is a multi-program laboratory managed and operated by Sandia Corporation, a wholly owned subsidiary of Lockheed Martin Corporation, for the U.S. Department of Energy's National Nuclear Security Administration under contract DE-AC04-94AL85000. The authors are thankful for support from the Army Research Office award no. W911NF-14-1-0250 and encouragement from our program manager, Dr Ralph Anthenien. Mr Logan Smith is gratefully acknowledged for assisting with experiments and data collection.

References

1 A. Varma, Form from fire, *Sci. Am.*, 2000, **283**(2), 58–61.
2 F. A. Williams, Observations on burning and flame-spread of black powder, *AIAA J.*, 1976, **14**(5), 637–643.
3 S. F. Son, B. W. Asay, T. J. Foley, R. A. Yetter, M. H. Wu and G. A. Risha, Combustion of Nanoscale Al/MoO_3 Thermite in Microchannels, *J. Propul. Power*, 2007, **23**(4), 715–721.
4 K. Kappagantula, C. Crane and M. Pantoya, Determination of the spatial temperature distribution from combustion products: a diagnostic study, *Rev. Sci. Instrum.*, 2013, **84**(10), 104902.
5 E. M. Hunt and M. L. Pantoya, Impact sensitivity of intermetallic nanocomposites: a study on compositional and bulk density, *Intermetallics*, 2010, **18**(8), 1612–1616.
6 K. T. Sullivan, M. A. Worsley, J. D. Kuntz and A. E. Gash, Electrophoretic deposition of binary energetic composites, *Combust. Flame*, 2012, **159**(6), 2210–2218.
7 A. Bacciochini, M. I. Radulescu, M. Yandouzi, G. Maines, J. J. Lee and B. Jodoin, Reactive structural materials consolidated by cold spray: Al–CuO thermite, *Surf. Coat. Technol.*, 2013, **226**, 60–67.

8 K. T. Sullivan, J. D. Kuntz and A. E. Gash, Electrophoretic deposition and mechanistic studies of nano-Al/CuO thermites, *J. Appl. Phys.*, 2012, **112**(2), 024316.

9 J. L. Cheng, H. H. Hng, H. Y. Ng, P. C. Soon and Y. W. Lee, Synthesis and characterization of self-assembled nanoenergetic Al–Fe_2O_3 thermite system, *J. Phys. Chem. Solids*, 2010, **71**(2), 90–94.

10 G. Jian, S. Chowdhury, K. Sullivan and M. R. Zachariah, Nanothermite reactions: is gas phase oxygen generation from the oxygen carrier an essential prerequisite to ignition?, *Combust. Flame*, 2013, **160**(2), 432–437.

11 D. Prentice, M. L. Pantoya and B. J. Clapsaddle, Effect of nanocomposite synthesis on the combustion performance of a ternary thermite, *J. Phys. Chem. B*, 2005, **109**(43), 20180–20185.

12 R. Armstrong, Models For Gasless Combustion in Layered Materials and Random Media, *Combust. Sci. Technol.*, 1990, **71**, 155–174.

13 K. A. Meeks, B. R. Clark, J. E. Cano, C. A. Apblett and M. L. Pantoya, Effects of rheological properties on reactivity of energetic thin films, *Combust. Flame*, 2015, **162**(9), 3288–3293.

14 K. Meeks, M. L. Pantoya and C. Apblett, Deposition and characterization of energetic thin films, *Combust. Flame*, 2014, **161**(4), 1117–1124.

15 C. Y. Ho, R. W. Powell and P. E. Liley, Thermal conductivity of the elements, *J. Phys. Chem. Ref. Data*, 1972, **1**(2), 351.

16 R. Fogelholm, O. Rapp and G. Grimvall, Electrical resistivity of indium: deviation from linearity at high temperatures, *Phys. Rev. B: Condens. Matter Mater. Phys.*, 1981, **23**(8), 3845–3851.

17 H. Kim, C. M. Gilmore, A. Piqué, J. S. Horwitz, H. Mattoussi, H. Murata, Z. H. Kafafi and D. B. Chrisey, Electrical, optical, and structural properties of indium tin oxide thin films for organic light-emitting devices, *J. Appl. Phys.*, 1999, **86**(11), 6451–6461.

18 D. V. Shenai, M. L. Timmons, R. L. Dicarlo and C. J. Marsman, Correlation of film properties and reduced impurity concentrations in sources for III/V-MOVPE using high-purity trimethylindium and tertiarybutylphosphine, *J. Cryst. Growth*, 2004, **272**, 603–608.

19 D. R. Frear and P. T. Vianco, Intermetallic Growth and Mechanical Behavior of Low and High Melting Temperature Solder Alloys, *Metall. Mater. Trans. A*, 1994, **25**, 1509–1523.

20 M. Abtew and G. Selvaduray, Lead-free solders in microelectronics, *Mater. Sci. Eng., R*, 2000, **27**(5), 95–141.

21 M. D. Dickey, R. C. Chiechi, R. J. Larsen, E. A. Weiss, D. A. Weitz and G. M. Whitesides, Eutectic gallium-indium (EGaIn): a liquid metal alloy for the formation of stable structures in microchannels at room temperature, *Adv. Funct. Mater.*, 2008, **18**(7), 1097–1104.

22 R. H. B. Bouma, D. Meuken, R. Verbeek, M. M. Pacheco and L. Katgerman, Shear Initiation of Al/MoO_3-Based Reactive Materials, *Propellants, Explos., Pyrotech.*, 2007, **32**(6), 447–453.

23 B. R. Clark, M. L. Pantoya, E. M. Hunt, T. J. Kelly, B. F. Allen, R. J. Heaps and M. A. Daniels, Synthesis and characterization of flexible, free-standing, energetic thin films, *Surf. Coat. Technol.*, 2015, **284**, 422–426.

24 A. Al-Harthi and A. Williams, Effect of fuel binder and oxidiser particle diameter on the combustion of ammonium perchlorate based propellants, *Fuel*, 1998, **77**(13), 1451–1468.

25 E. C. Koch, Metal-Fluorocarbon-Pyrolants: III. Development and Application of Magnesium/Teflon/Viton (MTV), *Propellants, Explos., Pyrotech.*, 2002, **27**(5), 262–266.

26 C. D. Yarrington, S. F. Son and T. J. Foley, Combustion of Silicon/Teflon/Viton and Aluminum/Teflon/Viton Energetic Composites, *J. Propul. Power*, 2010, **26**(4), 734–743.

27 E. Vidal, J. M. Rojo, M. C. García-Alegre, D. Guinea, E. Soto and J. M. Amarilla, Effect of composition, sonication and pressure on the rate capability of 5V–$LiNi_{0.5}Mn_{1.5}O_4$ composite cathodes, *Electrochim. Acta*, 2013, **108**, 175–181.

28 E. S. Collins, B. R. Skelton, M. L. Pantoya, F. Irin, M. J. Green and M. A. Daniels, Ignition sensitivity and electrical conductivity of an aluminum fluoropolymer reactive material with carbon nanofillers, *Combust. Flame*, 2015, **162**(4), 1417–1421.

29 E. Vargas, M. L. Pantoya, M. A. Saed and B. L. Weeks, Advanced susceptors for microwave heating of energetic materials, *Mater. Des.*, 2016, **90**, 47–53.

30 K. Kappagantula and M. L. Pantoya, Experimentally measured thermal transport properties of aluminum–polytetrafluoroethylene nanocomposites with graphene and carbon nanotube additives, *Int. J. Heat Mass Transfer*, 2012, **55**(4), 817–824.

31 D. K. Smith and M. L. Pantoya, Effect of nanofiller shape on effective thermal conductivity of fluoropolymer composites, *Compos. Sci. Technol.*, 2015, **118**, 251–256.

32 R. Zallen and H. Scher, Percolation on a continuum and the localization–delocalization transition in amorphous semiconductors, *Phys. Rev. B: Condens. Matter Mater. Phys.*, 1971, **4**(12), 4471–4479.

33 E. Gawlinski and H. Stanley, Continuum percolation in two dimensions: Monte Carlo tests of scaling and universality for non-interacting discs, *J. Phys. A: Math. Gen.*, 1981, **14**(8), L291–L299.

34 F. Irin, S. Das, F. O. Atore and M. J. Green, Ultralow percolation threshold in aerogel and cryogel templated composites, *Langmuir*, 2013, **29**(36), 11449–11456.

35 J. C. Grunlan, W. W. Gerberich and L. F. Francis, Lowering the percolation threshold of conductive composites using particulate polymer microstructure, *J. Appl. Polym. Sci.*, 2001, **80**(4), 692–705.

36 M. J. Biercuk, M. C. Llaguno, M. Radosavljevic, J. K. Hyun, A. T. Johnson and J. E. Fischer, Carbon nanotube composites for thermal management, *Appl. Phys. Lett.*, 2002, **80**(15), 2767–2769.

37 S. Duwe, C. Arlt, S. Aranda, U. Riedel and G. Ziegmann, A detailed thermal analysis of nanocomposites filled with SiO_2, AlN or boehmite at varied contents and a review of

selected rules of mixture, *Compos. Sci. Technol.*, 2012, **72**(12), 1324–1330.
38 L. Nielsen, Polymeric Composite Systems with two continuous phases, *J. Appl. Polym. Sci.*, 1977, **21**(6), 1579–1584.
39 S. H. Fischer and M. C. Grubelich, Theoretical Energy Release of Thermites, Intermetallics, and Combustible Materials, in *24th Intl. Pyrotechnics Seminar*, 1998.
40 W. J. Parker, R. J. Jenkins, C. P. Butler and G. L. Abbott, Flash method of determining thermal diffusivity, heat capacity, and thermal conductivity, *J. Appl. Phys.*, 1961, **32**(9), 1679–1684.
41 G. V. Belov, Thermodynamic Analysis of Combustion Products at High Temperature and Pressure, *Propellants, Explos., Pyrotech.*, 1998, **23**, 86–89.
42 Z. Hashin and S. Shtrikman, A variational approach to the theory of the elastic behaviour of multiphase materials, *J. Mech. Phys. Solids*, 1963, **11**(2), 127–140.
43 Z. Hashin and S. Shtrikman, A variational approach to the theory of the elastic behaviour of polycrystals, *J. Mech. Phys. Solids*, 1962, **10**(4), 343–352.
44 S. Walia, S. Balendhran, P. Yi, D. Yao, S. Zhuiykov, M. Pannirselvam, R. Weber, M. S. Strano, M. Bhaskaran, S. Sriram and K. Kalantar-Zadeh, MnO_2-based thermopower wave sources with exceptionally large output voltages, *J. Phys. Chem. C*, 2013, **117**(18), 9137–9142.
45 R. W. Powell, C. Y. Ho and P. E. Liley, Thermal conductivity of selected materials, *Natl. Stand. Ref. Data Ser.*, 1966, **8**, 93–96.
46 B. Weidenfeller, M. Höfer and F. Schilling, Thermal and electrical properties of magnetite filled polymers, *Composites, Part A*, 2002, **33**(8), 1041–1053.
47 F. R. Schilling and G. M. Partzsch, Quantifying partial melt fraction in the crust beneath and Central Andes and the Tibetan Plateau, *Physics and Chemistry of the Earth, Part A: Solid Earth and Geodesy*, 2001, **26**(4–5), 239–246.
48 H. Scher and R. Zallen, Critical Density in Percolation Processes, *J. Chem. Phys.*, 1970, **53**(9), 3759–3761.
49 S. Mertens and C. Moore, Continuum percolation thresholds in two dimensions, *Phys. Rev. E: Stat., Nonlinear, Soft Matter Phys.*, 2012, **86**(6), 061109.
50 J. Quintanilla, S. Torquato and R. M. Ziff, Efficient measurement of the percolation threshold for fully penetrable discs, *J. Phys. A: Math. Gen.*, 2000, **33**(42), L399–L407.
51 I. Balberg, 'Universal' percolation threshold limits in the continuum, *Phys. Rev. B: Condens. Matter Mater. Phys.*, 1985, **31**(6), 4053–4055.
52 K. Meeks, M. L. Pantoya, M. Green and J. Berg, Extending the excluded volume for percolation threshold estimates in polydisperse systems: The binary disk system, *Applied Mathematical Modelling*, 2017, **46**, 116–125.
53 K. Meeks, J. Tencer and M. L. Pantoya, Percolation of binary disk systems: modeling and theory, *Phys. Rev. E: Stat., Nonlinear, Soft Matter Phys.*, 2017, **95**(1), 012118.
54 V. E. Sanders, B. W. Asay, T. J. Foley, B. C. Tappan, A. N. Pacheco and S. F. Son, Reaction Propagation of Four Nanoscale Energetic Composites (Al/MoO_3, Al/WO_3, Al/CuO, and $B_{12}O_3$), *J. Propul. Power*, 2007, **23**(4), 707–714.
55 H. Wu, X. Wu, M. Ge, G. Zhang, Y. Wang and J. Jiang, Effect analysis of filler sizes on percolation threshold of isotropical conductive adhesives, *Compos. Sci. Technol.*, 2007, **67**(6), 1116–1120.
56 L. Z. Zhang, X. J. Wang, Y. Y. Quan and L. X. Pei, Conjugate heat conduction in filled composite materials considering interactions between the filler and base materials, *Int. J. Heat Mass Transfer*, 2013, **64**, 735–742.
57 S. Zhang, X. Y. Cao, Y. M. Ma, Y. C. Ke, J. K. Zhang and F. S. Wang, The effects of particle size and content on the thermal conductivity and mechanical properties of Al_2O_3/high density polyethylene (HDPE) composites, *eXPRESS Polym. Lett.*, 2011, **5**(7), 581–590.
58 H. Im and J. Kim, The effect of Al_2O_3 doped multi-walled carbon nanotubes on the thermal conductivity of Al_2O_3/epoxy terminated poly(dimethylsiloxane) composites, *Carbon*, 2011, **49**(11), 3503–3511.
59 Z. Birčáková, P. Kollár, B. Weidenfeller, J. Füzer, M. Fáberová and R. Bureš, Reversible and irreversible DC magnetization processes in the frame of magnetic, thermal and electrical properties of Fe-based composite materials, *J. Alloys Compd.*, 2015, **645**, 283–289.